Electronic Supplementary Material (ESI) for Journal of Materials Chemistry A.

Supplementary information for

Spin-engineered Cu-Ni metallic aerogels for enhanced ethylamine electrosynthesis from acetonitrile

Honggang Huang,[a] Feili Lai,[b] Hui Fu,[a] Yao Chen,[a] Hanjun Li,[a] Feng He,[c] Zhenyu Wang,[c] Nan Zhang,*[a] Shuxing Bai*[d] and Tianxi Liu*[a]

[a] Key Laboratory of Synthetic and Biological Colloids, Ministry of Education, School of Chemical and Material Engineering, International Joint Research Laboratory for Nano Energy Composites, Jiangnan University, Wuxi, 214122, China.

[b] Department of Chemistry, KU Leuven, Celestijnenlaan 200F, Leuven 3001, Belgium.

[c] Institute of Environmental Processes and Pollution control, and School of Environment and Civil Engineering, Jiangnan University, Wuxi 214122, China

[d] College of Chemistry and Chemical Engineering, Qingdao University, Qingdao, 266071, China.

E-mail: nzhang@jiangnan.edu.cn, shuxbai@qdu.edu.cn, txliu@jiangnan.edu.cn

Experimental section:

Chemicals. Nickel(II) chloride hexahydrate ($NiCl_2·6H_2O$), sodium borohydride ($NaBH_4$), sodium hydroxide (NaOH) and ammonium chloride (NH_4Cl) were purchased from Sinopharm Chemical Reagent Co. Ltd (Shanghai, China). Copper(II) chloride ($CuCl_2$), ethylamine (C_2H_7N), and acetonitrile (C_2H_3N) were purchsaed from Titan Chemical Co. Ltd (Shanghai, China). Sodium citrate (NaCA) was purchased from Innochem Technology Co. Ltd (Beijing, China). The water (H_2O) (18 MΩ cm^{-1}) used in all experiments was prepared by passing through an ultra-pure purification system (Aqua Solutions).

Synthesis of Cu-Ni metallic aerogels (MAs). In a typical synthesis of Cu-Ni MAs, hydrogels were synthesized by an NH_4Cl-induced gelation. By taking the preparation of the Cu-Ni (1:1) hydrogel as an example, NaCA (15 mmol, 3.871 g), $NiCl_2·6H_2O$ (0.5 mmol, 118.845 mg), $CuCl_2$ (0.5 mmol, 67.225 mg), and $NaBH_4$ (20 mmol, 756.6 mg) were successively added into 300 mL water under stirring. Then, NH_4Cl (10 mmol, 534.9 mg) was added into the as-prepared solution (300 mL) followed by grounding for ~6 h to form a monolithic Cu-Ni hydrogel. The ratio of Cu to Ni in the Cu-Ni hydrogel was controlled by tuning the molar ratio of $CuCl_2$ and $NiCl_2·6H_2O$. $NiCl_2·6H_2O$ (0.25 mmol, 59.42 mg), $CuCl_2$ (0.75 mmol, 100.84

mg) were used for Cu-Ni (3:1) hydrogel; $NiCl_2 \cdot 6H_2O$ (0.75 mmol, 178.27 mg), $CuCl_2$ (0.25 mmol, 33.61 mg) were used for Cu-Ni (1:3) hydrogel; $CuCl_2$ (1 mmol, 134.45 mg) was used for Cu hydrogel and $NiCl_2 \cdot 6H_2O$ (1 mmol, 237.69 mg) was used for Ni hydrogel. The resulting hydrogels were purified with water for 4~5 times. Afterwards, the wet gels were dried via a freeze-drying method for 12 h.

Synthesis of Cu_3Ni_1 nanoparticles (NPs). The obtained Cu_3Ni_1 hydrogels were dried via vacuum drying oven at 80 ºC for 12 h to prepare the Cu_3Ni_1 NPs.

Characterization. The transmission electron microscopy (TEM) samples were prepared by dropping ethanol dispersion of samples on carbon-coated copper grids using pipettes and dried under ambient condition. Low-magnification TEM images were collected on a JEM-2100plus transmission electron microscope with applying an acceleration voltage of 200 kV. High-magnification TEM, element mapping images and scanning TEM (STEM) images were collected on a JEOL JEM 2100F TEM with an acceleration voltage of 200 kV. X-ray diffraction (XRD) patterns were collected by Linx array detector (Germany Brooke) with a Cu Kα X-ray source (λ= 1.540598 Å). Scanning electron microscopy energy-dispersive X-ray spectroscopy (SEM-EDS) spectra were taken with a HITACHI S-4800 cold field emission scanning electron microscope. X-ray photoelectron spectroscopy (XPS) was performed on Thermo Scientific K-Alpha XPS Spectrometer. The carbon peak at 284.8 eV is used as a reference to correct the charging effects. Fourier infrared spectrometer (IR) spectra and the absorbance data were recorded in the spectral region of 500-4000 nm with Fourier infrared spectrometer (Nicolet iS50 FT-IR,). Magnetization hysteresis loops (VSM) were performed on Quantum Design VersaLab. 400 MHz nuclear magnetic resonance (NMR) spectroscopy (AVANCE III HD) was used to identify and quantify the yield of products in liquid electrolyte. Automatic specific surface area and microporous physical adsorption instrument (BET) was used to calculate the specific surface area and pore size distribution of the material. The in-situ Raman spectroelectrochemical experiments were performed by HORIBA/XploRA PLUS. Excitation radiation at 638 nm from a He/Ne laser coherent was used. The in-situ Raman spectroelectrochemical experiments were performed under constant cathodic potentials progressively stepping to negative limits from the open-circuit potential (OCP).

Electrochemical measurement.

H-cell system. The electrochemical measurements of acetonitrile reduction reaction (ARR) were conducted in a three-electrode cell using a CHI 660e. The electrochemical measurement was conducted in a typical H-cell tank with the anion exchange membrane (Nafion 211). Ag/AgCl (3 M KCl) and carbon rod were used as reference electrode and counter electrode. For the working electrode, 995 μL of isopropanol and 5 μL of Nafion solution (5 wt%) were used to disperse 10 mg catalysts to form homogeneous ink. Then, 10 μL of the ink was doped onto the glassy carbon electrode and dried at room temperature to obtain the working electrode. The cathode electrolytic cell contained 30 mL 8 wt.% acetonitrile in 1 M NaOH solution and anode electrolytic cell contained 30 mL 1 M NaOH solution.

Calibration of Ag/AgCl electrode. We used a three-electrode system, for Ag/AgCl electrode as the reference electrode and two Pt wires as the working electrode and counter electrode respectively. The same electrolyte (8 wt% acetonitrile in 1 M NaOH) was used. Before the test, high-purity hydrogen was applied for 30 min to saturate the hydrogen content dissolved in the electrolyte. During the test, high-purity hydrogen was continued to be applied to the Pt wires electrode, then we conducted the linear scanning voltammetry (LSV) test at a sweep rate of 5 mV s^{-1}, repeating for three times. The zero current is the correction potential. Through taking the average value of the corresponding potential of the three zero current points, it could be obtained that $E_{RHE}=E_{Ag/AgCl}$ + average value.

Flow cell system. The commercial-scale activity of as-prepared Cu_3Ni_1 MAs and Cu_3Ni_1 NPs were evaluated by using membrane electrode assembly (MEA) with proton-exchange membrane (PEM). The cell included two end plates, on which a single serpentine flow field (6.25 cm^2 area, 1.0 mm width, 0.5 mm depth) was machined. To fabricate cathode electrodes, the catalyst (5 mg) was dispersed in a suspension of Nafion (5 wt%) (100 μL), isopropanol (9.9 mL), and then spray coated onto carbon paper (6.25 cm^2). The catalysts loading on the as-prepared electrode was 0.8 mg cm^{-2}. The anode electrode is Ni foam, a known durable catalyst. A Nafion 211 PEM was used in flow cell system, placed between the anode and cathode electrode. And then 1 M NaOH with 8wt% acetonitrile were pumped into the cathode electrode channel, while 1 M NaOH was for anode electrode channel by a peristaltic pump.

Product analysis. For the liquid product, ^{1}H NMR was conducted on AVANCE Ⅲ HD 400 MHz spectrometers. In short, 1 mL of the sampled catholyte was added with 200 μL of D_2O and 100 μL of 1000 ppm DMSO. Wherein, D_2O and DMSO are used as deuterated solvent and internal standard solution respectively. The standard curve of ethylamine in ^{1}H-NMR tests by the peak area ratio of ethylamine and DMSO at different concentrations. The ratio of ethylamine and DMSO in the electrolyte is calculated through the ^{1}H-NMR of the electrolyte after the electrochemical tests, and then it is substituted into the standard curve of ethylamine to obtain the yield of ethylamine in the electrolyte.

The Faraday efficiency (FE) and yield rate are calculated by the following equation:

$$FE = eF \times n/Q$$

$$\text{Yield rate} = n/t$$

where e is the electrons transfer number and Q is the total charge. n and F are the total moles of the different product and Faraday constant, respectively. t is the reduction time.

Density functional theory (DFT) calculations. We have employed the Vienna ab initio simulation package (VASP)[1, 2] to perform all density functional theory (DFT) calculations within the generalized gradient approximation (GGA) using the Perdew-Burke-Ernzerhof (PBE)[3] formulation. We have chosen the projected augmented wave (PAW) potentials[4] to describe the ionic cores and take valence electrons into account using a plane wave basis set with a kinetic energy cutoff of 400 eV. Partial occupancies of the Kohn-Sham orbitals were allowed using the Gaussian smearing method and a width of 0.05 eV. The electronic energy was considered self-consistent when the energy change was smaller than 10^{-5} eV. A geometry optimization was considered convergent when the force change was smaller than 0.05 eV/Å. Grimme's DFT-D3 methodology[5] was used to describe the dispersion interactions. The Brillourin zone was sampled with a gamma-centered grid 2×2×1 through all the computational process.[6] Periodic boundary conditions were used in all directions and a vacuum layer of 15 Å was used in the *z*-direction to separate the slabs. The Cu_3Ni_1 structure of the aerogel configuration, we expanded 4×4×3 supercell through the bulk structure, and then built the pores inside.

The adsorption energy (E_{ads}) of adsorbate molecule was defined as

$$E_{ads} = E_{mol/surf} - E_{surf} - E_{mol}$$

where $E_{mol/surf}$, E_{surf} and E_{mol} are the energy of adsorbate molecule adsorbed on the surface, the energy of clean surface, and the energy of molecule respectively.

Supporting Figures and Table.

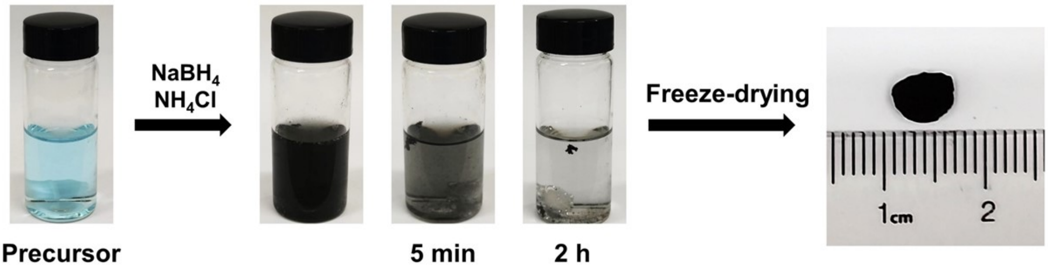

Fig. S1. Synthetic process of Cu_3Ni_1 MAs.

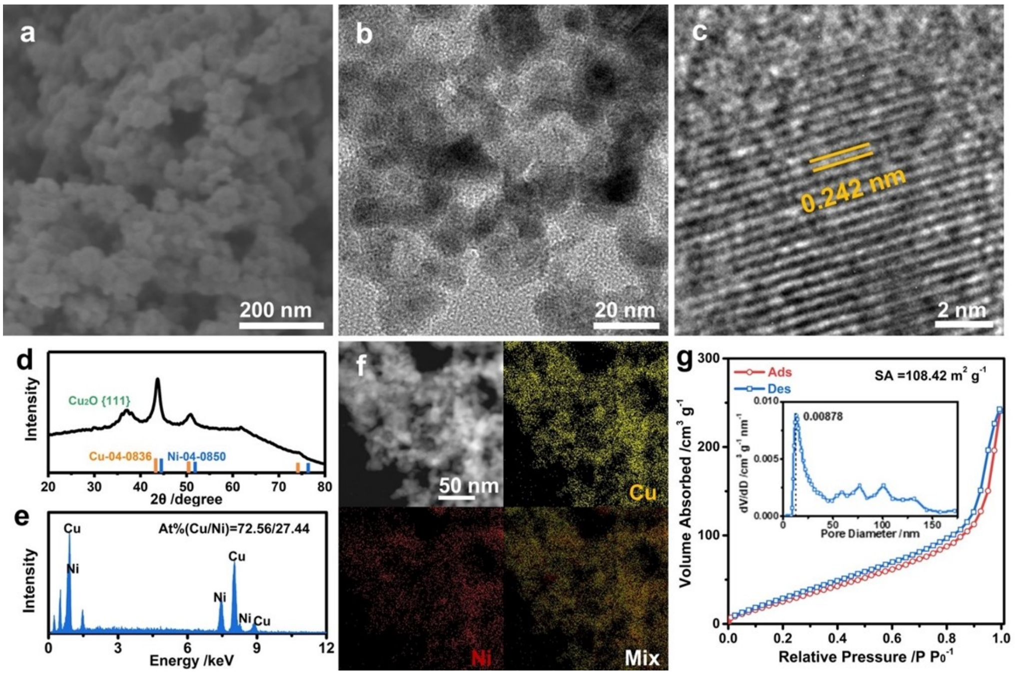

Fig. S2. (a) SEM image, (b) TEM image, (c) HRTEM image, (d) PXRD pattern, (e) SEM-EDS spectrum, (f) STEM image and corresponding elemental mappings, (g) nitrogen-sorption isotherms and pore diameter distribution of Cu_3Ni_1 NPs.

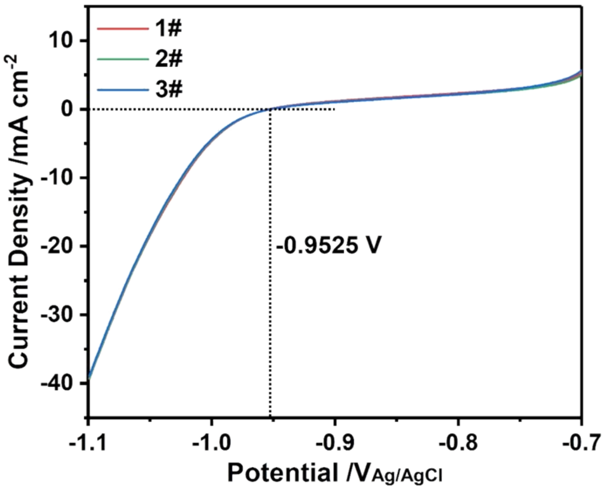

Fig. S3. Calibrations of Ag/AgCl electrode in 1 M NaOH with 8wt.% acetonitrile, $E_{RHE}=E_{Ag/AgCl}+0.9525$.

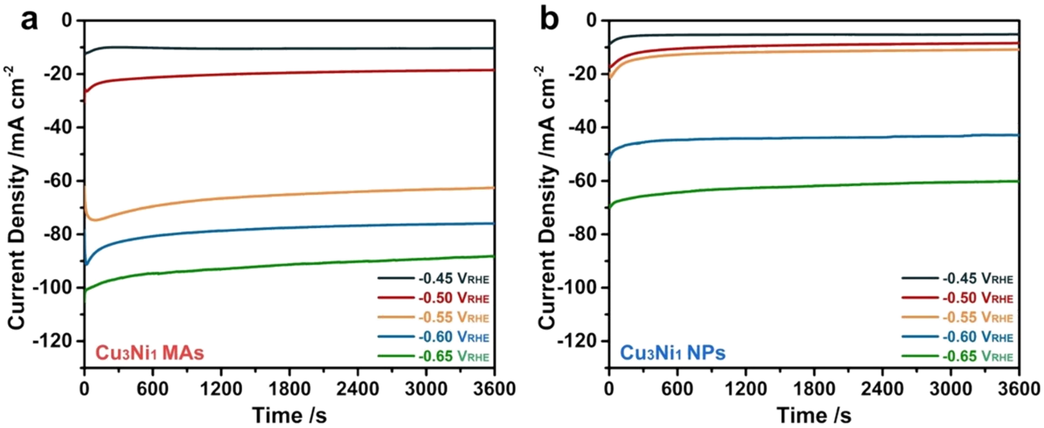

Fig. S4. Chronoamperometry curves during electrolysis on (a) Cu_3Ni_1 MAs and (b) Cu_3Ni_1 NPs at various applied potentials.

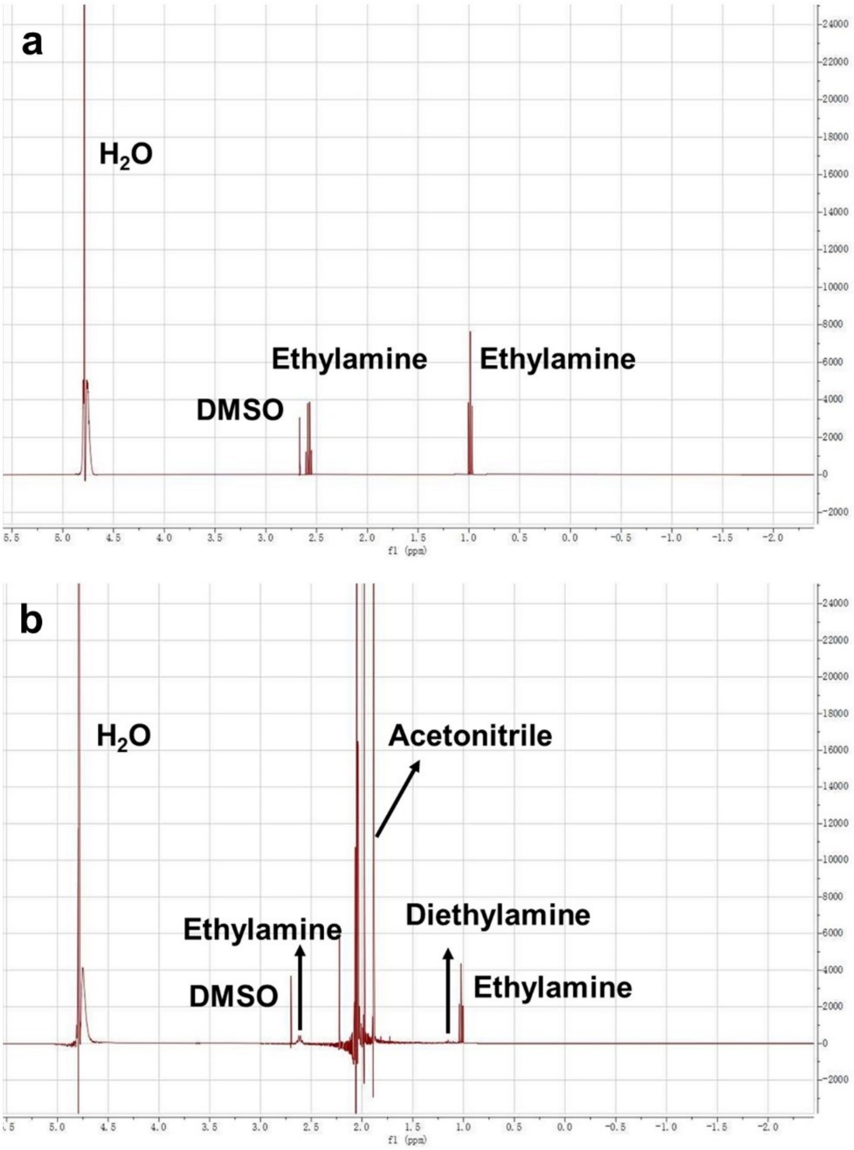

Fig. S5. ^1H NMR spectra of (a) ethylamine standard solution and (b) effluent electrolyte after ARR by Cu_3Ni_1 MAs at -0.65 V_{RHE} for 1 h.

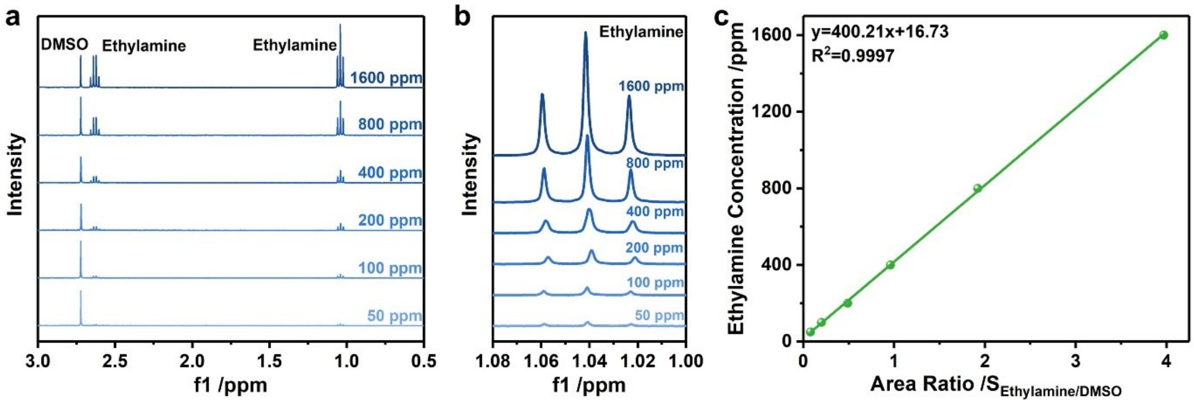

Fig. S6. (a,b) ^{1}H nuclear magnetic resonance (^{1}H-NMR) spectra of ethylamine and (c) standard curve of ethylamine. The standard curve of ethylamine shows the good linear relationship and follow the linear equation: y=400.21x+16.73.

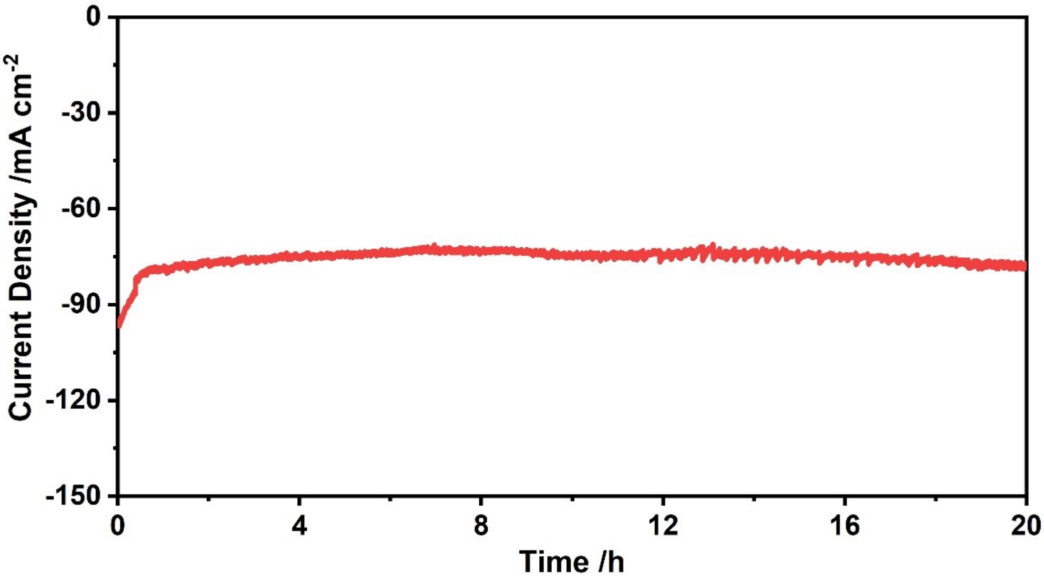

Fig. S7. Durability test of Cu_3Ni_1 MAs at -0.65 V_{RHE} for 20 h.

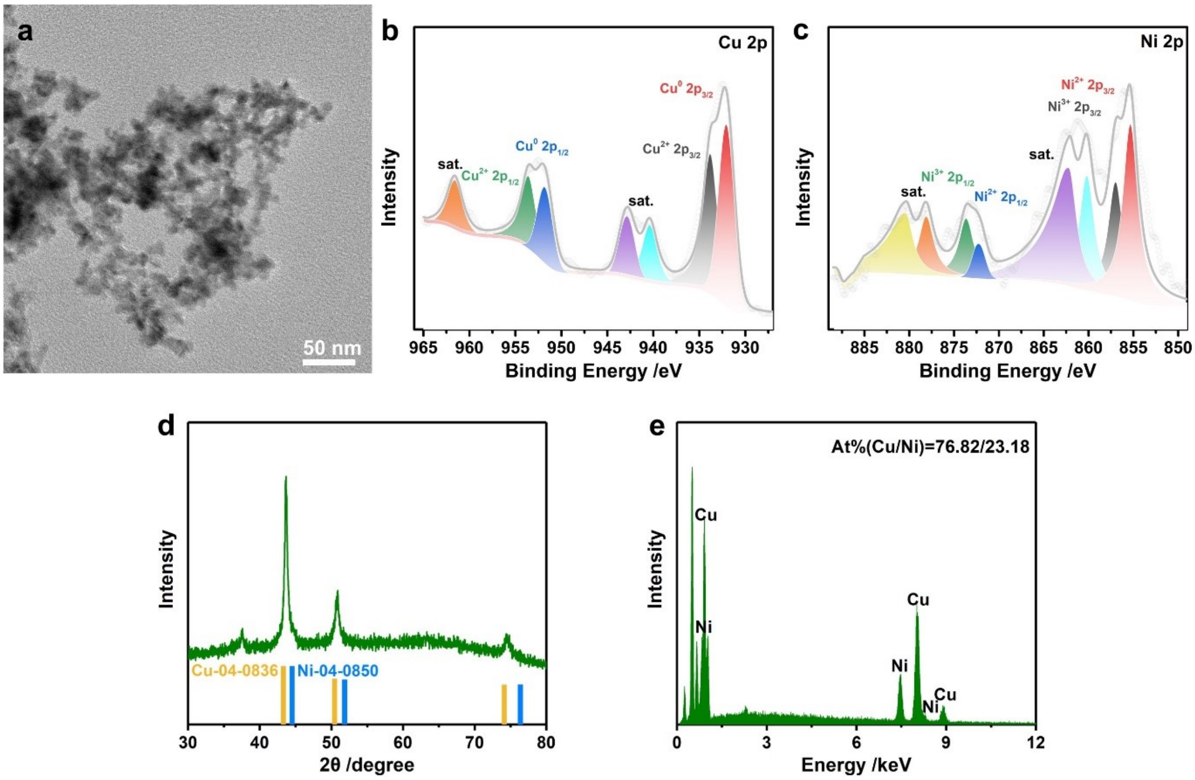

Fig. S8. (a) TEM image, (b) Cu 2p spectrum, (c) Ni 2p spectrum of Cu_3Ni_1 MAs, (d) PXRD pattern and (e) SEM-EDS spectrum after electrochemical test.

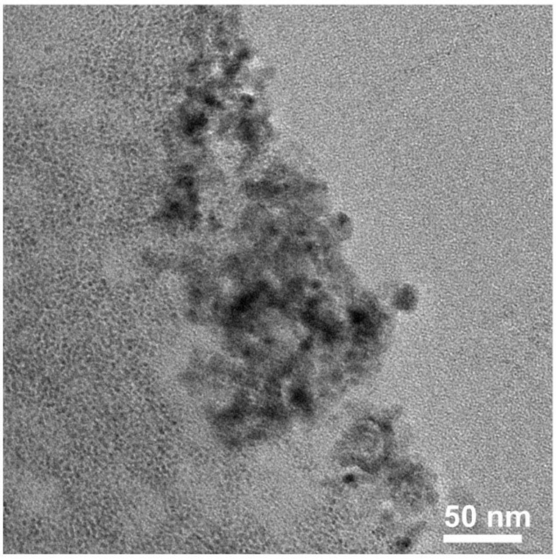

Fig. S9. TEM image of Cu_3Ni_1 NPs after electrochemical test.

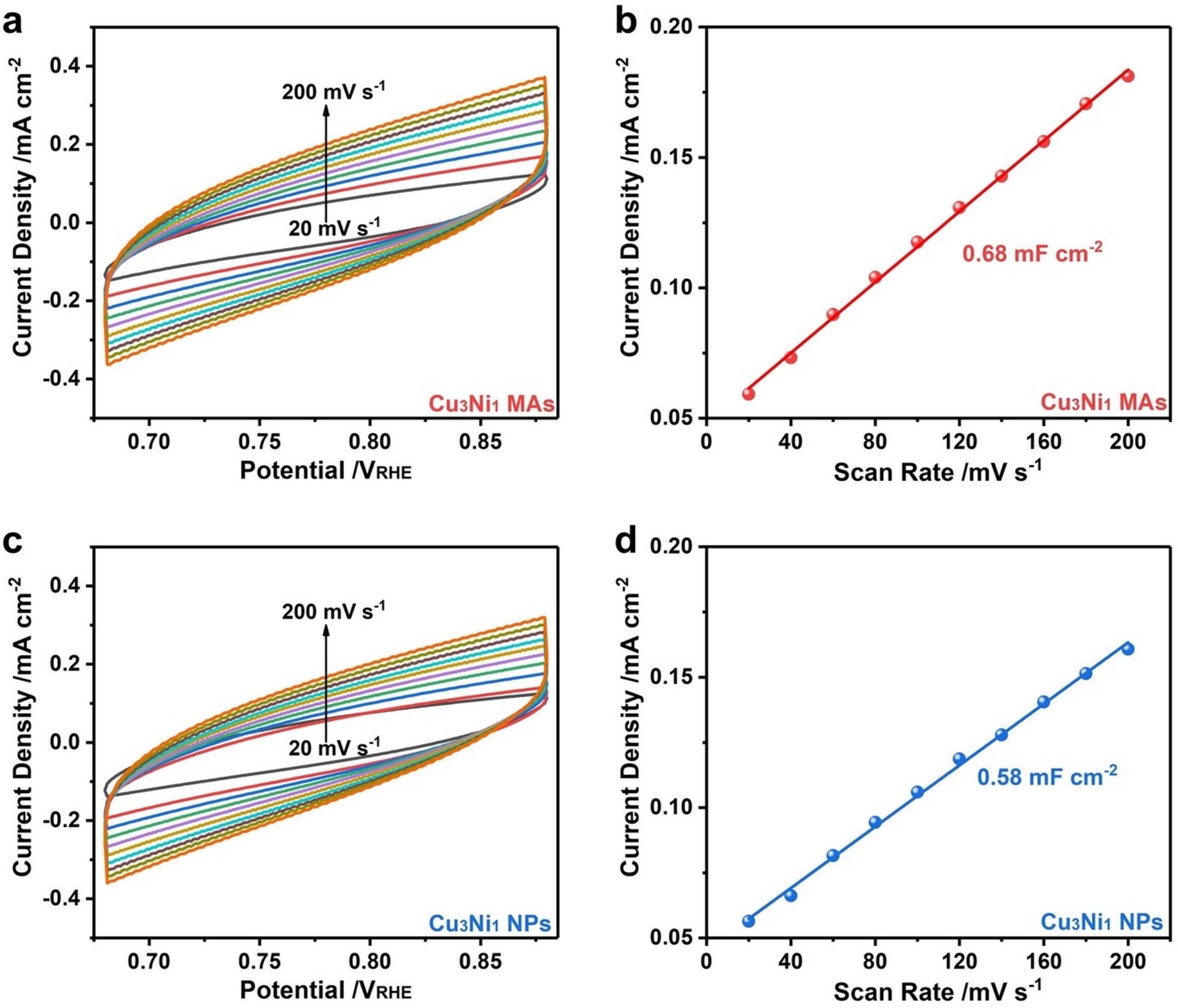

Fig. S10. Cyclic voltammograms measured from 20 mV s^{-1} to 200 mV s^{-1} of (a) the Cu_3Ni_1 MAs and (c) Cu_3Ni_1 NPs, and (b, d) corresponding double layer current density vs. scan rates plots.

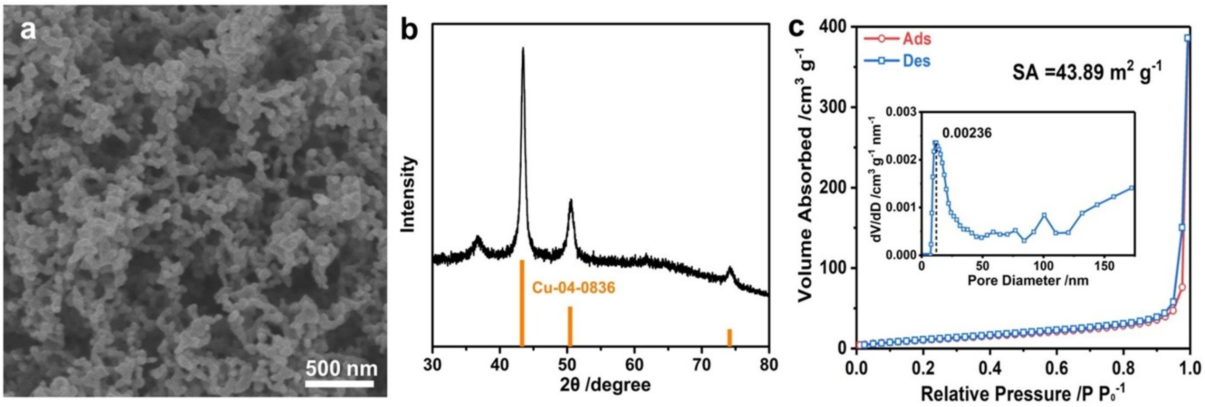

Fig. S11. (a) SEM image, (b) PXRD pattern, (c) nitrogen-sorption isotherms and pore diameter distribution of Cu MAs.

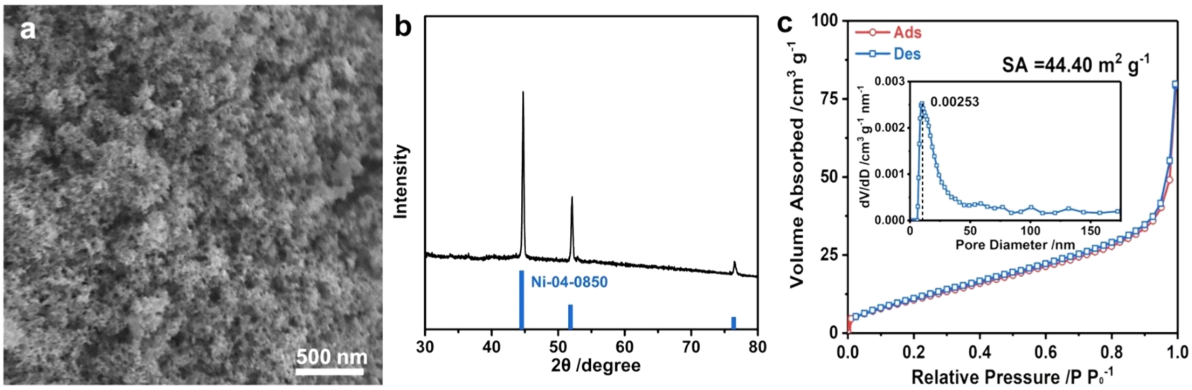

Fig. S12. (a) SEM image, (b) PXRD pattern, (c) nitrogen-sorption isotherms and pore diameter distribution of Ni MAs.

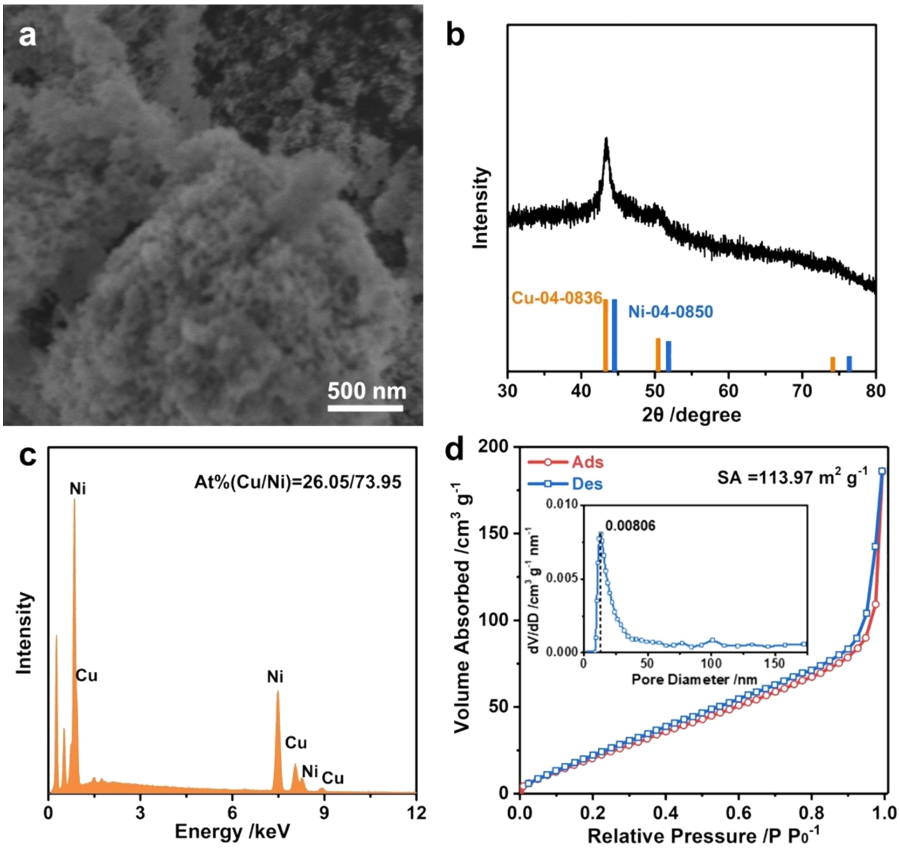

Fig. S13. (a) SEM image, (b) PXRD pattern, (c) SEM-EDS spectrum, (d) nitrogen-sorption isotherms and pore diameter distribution of Cu_1Ni_3 MAs.

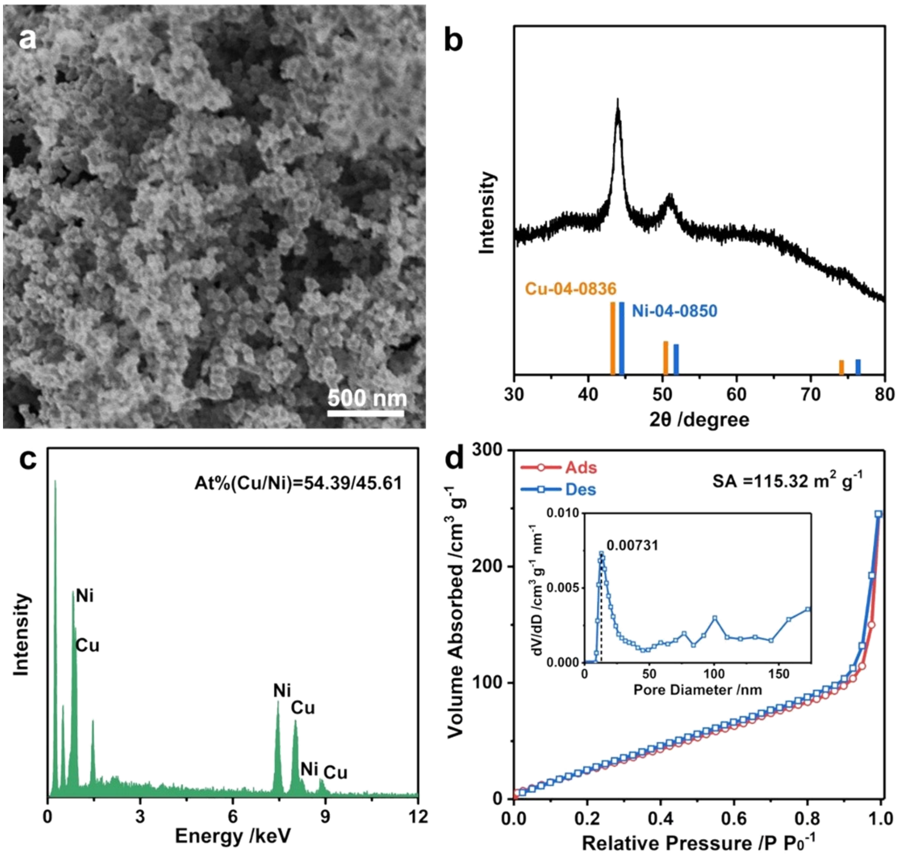

Fig. S14. (a) SEM image, (b) PXRD pattern, (c) SEM-EDS spectrum, (d) nitrogen-sorption isotherms and pore diameter distribution of Cu_1Ni_1 MAs.

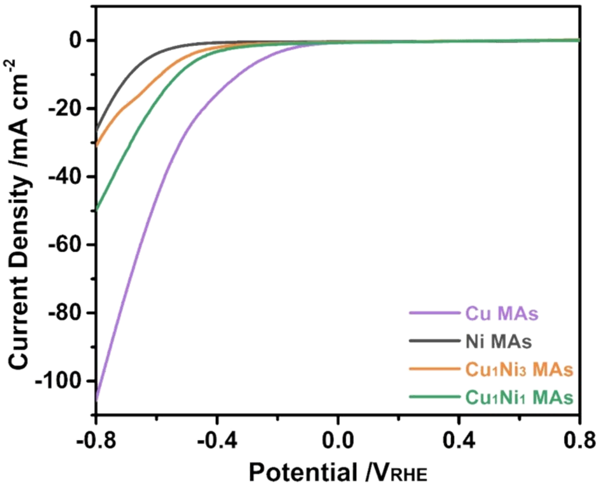

Fig. S15. LSV curves of Cu MAs, Ni MAs, Cu_1Ni_3 MAs and Cu_1Ni_1 MAs in 1 M NaOH with 8wt.% acetonitrile.

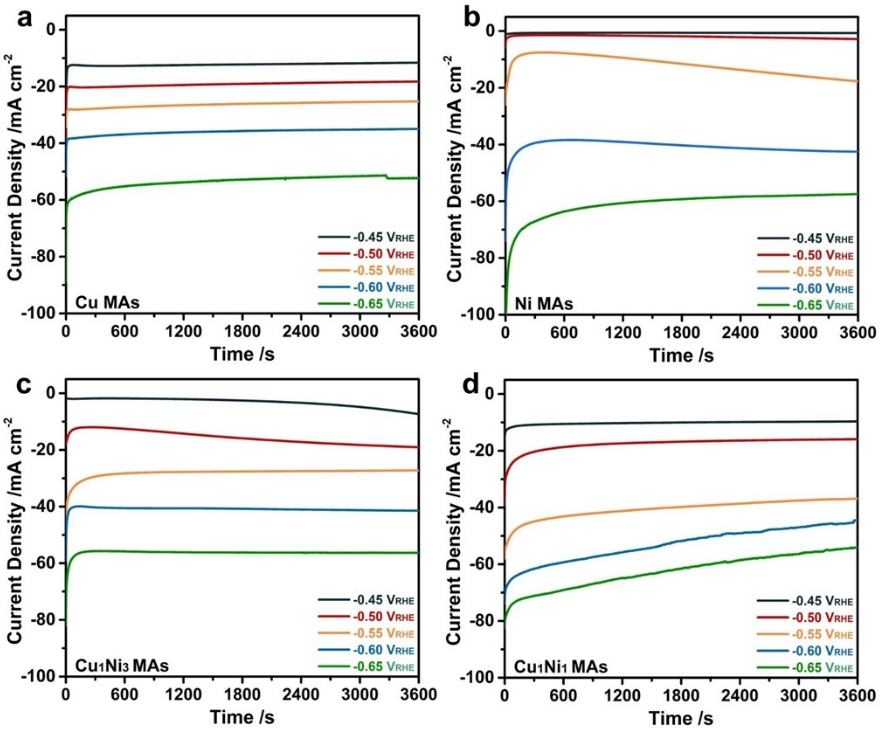

Fig. S16. Chronoamperometry curves during electrolysis on (a) Cu MAs, (b) Ni MAs, (c) Cu_1Ni_3 MAs, and (d) Cu_1Ni_1 MAs at various applied potentials.

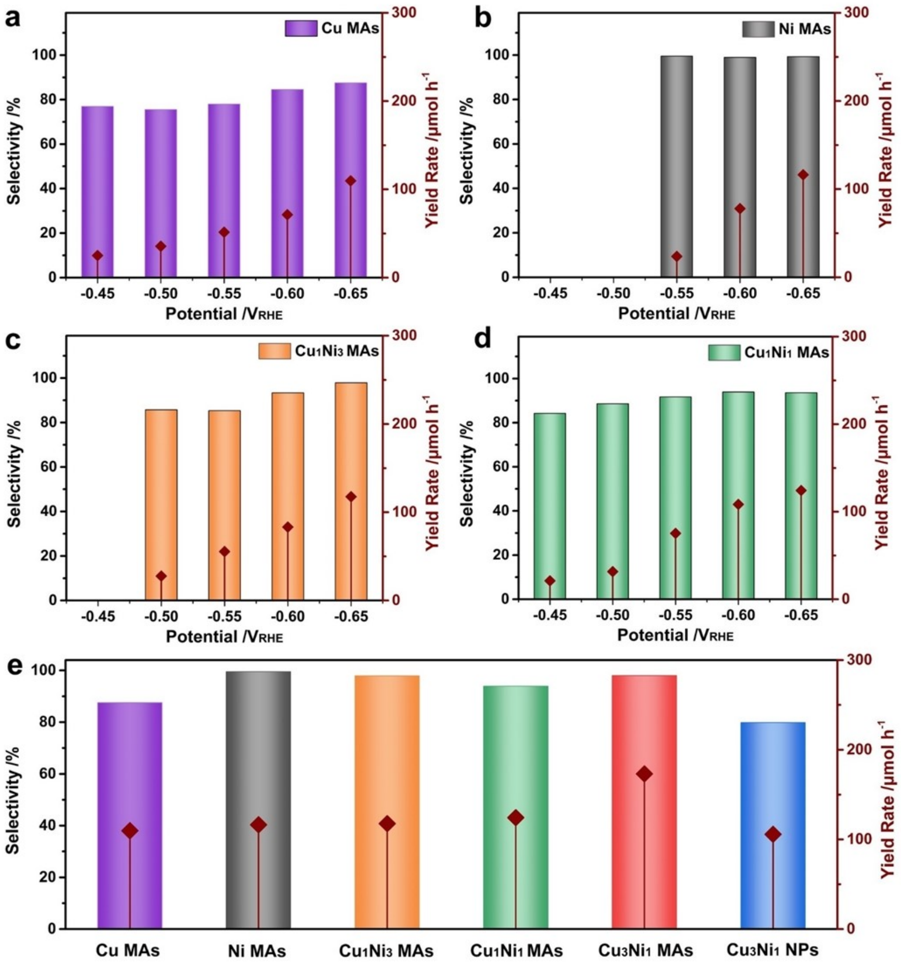

Fig. S17. Selectivity and yield rate of ethylamine on (a) Cu MAs, (b) Ni MAs, (c) Cu_1Ni_3 MAs and (d) Cu_1Ni_1 MAs at various applied potentials. (e) Selectivity and yield rate of ethylamine over the different catalysts at -0.65 V_{RHE}.

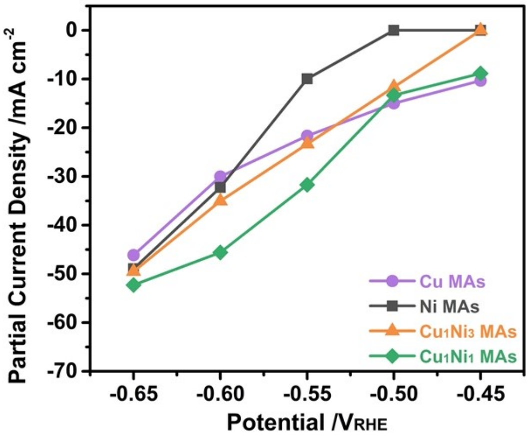

Fig. S18. Partial current densities of ethylamine over Cu MAs, Ni MAs, Cu_1Ni_3 MAs and Cu_1Ni_1 MAs.

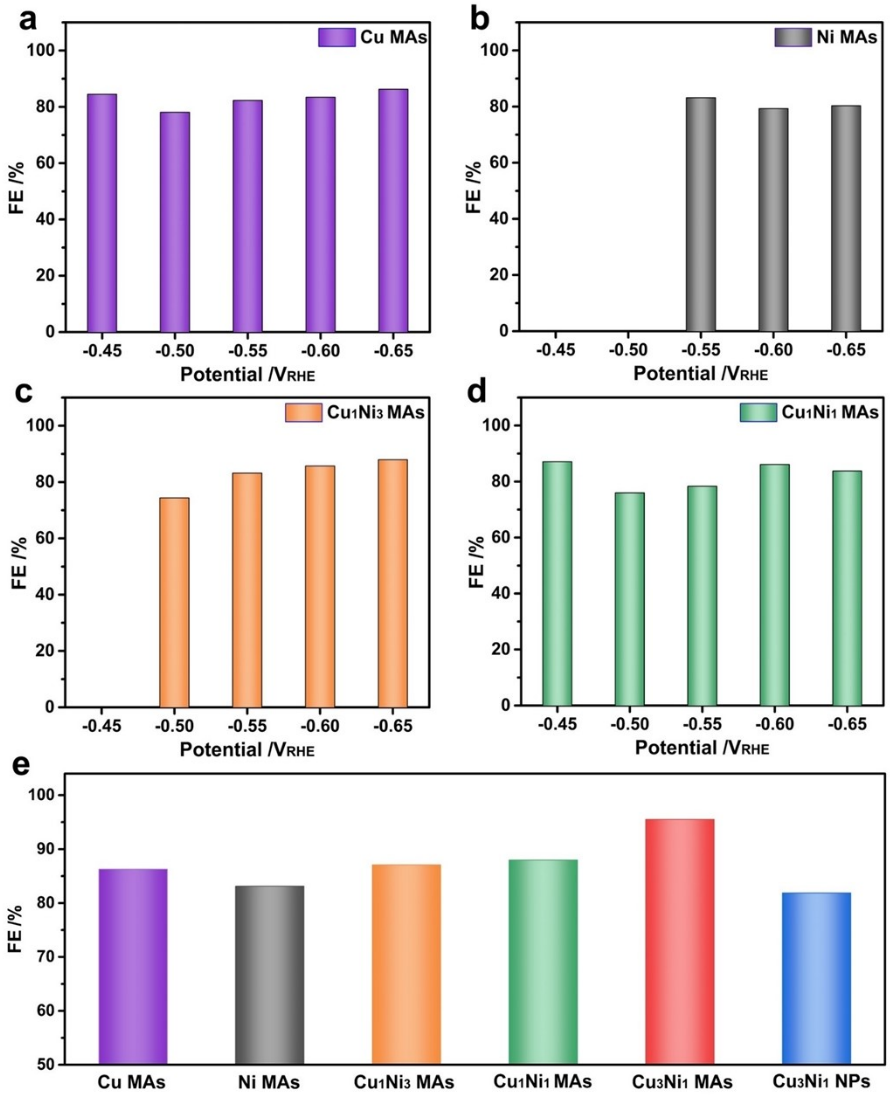

Fig. S19. Ethylamine FE on (a) Cu MAs, (b) Ni MAs, (c) Cu$_1$Ni$_1$ MAs and (d) Cu$_1$Ni$_3$ MAs at various applied potentials. (e) Highest ethylamine FE of each catalyts.

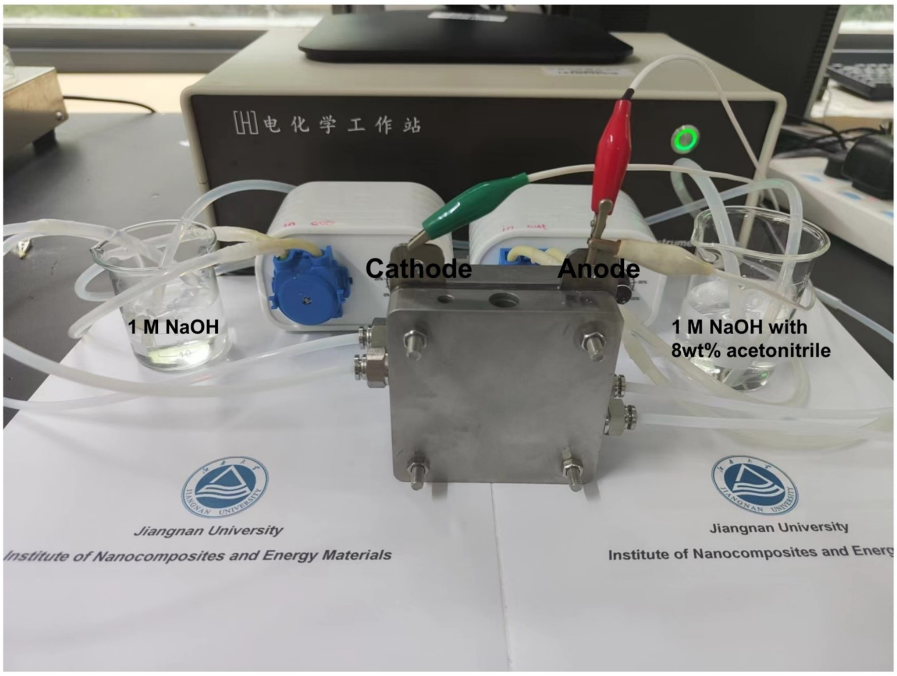

Fig. S20. Photo image of flow cell system.

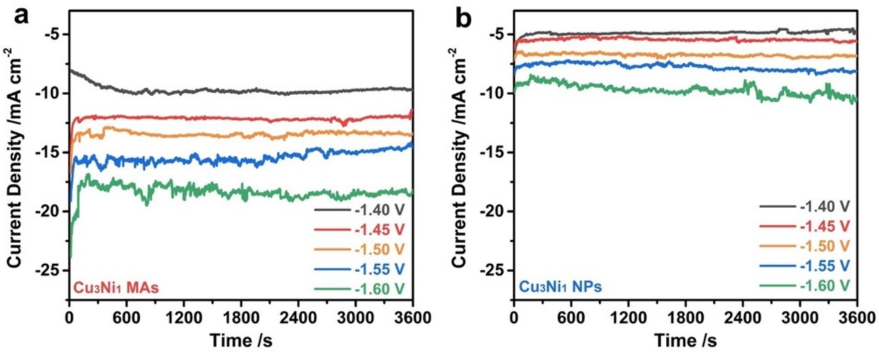

Fig. S21. Chronoamperometry curves during electrolysis on (a) Cu_3Ni_1 MAs and (b) Cu_3Ni_1 NPs in flow cell at various applied potentials.

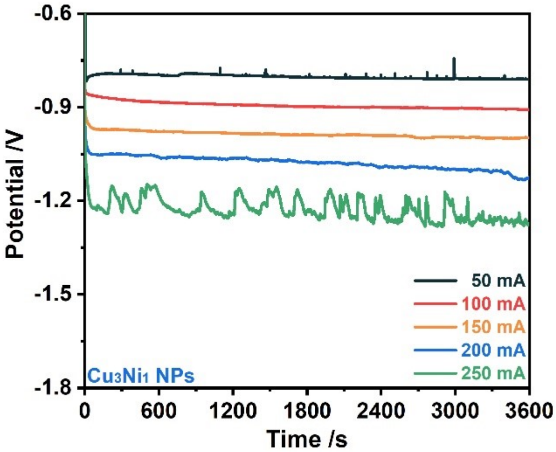

Fig. S22. Constant current mode of Cu_3Ni_1 NPs from 50 mA to 250 mA.

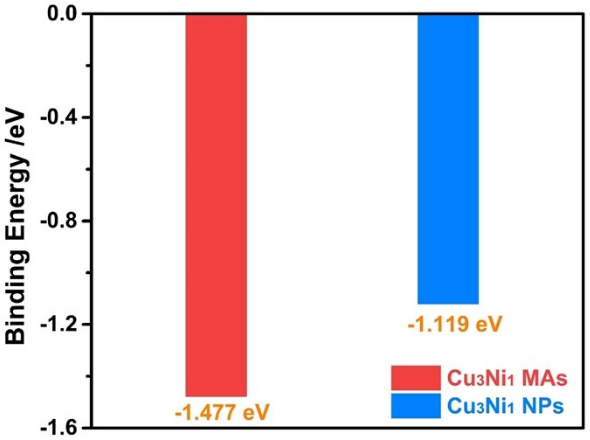

Fig. S23. Binding energy of acetonitrile on Cu_3Ni_1 MAs and Cu_3Ni_1 NPs.

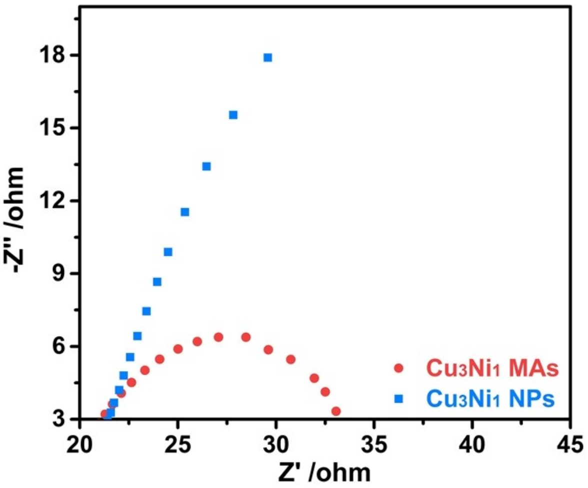

Fig. S24. Nyquist plots of Cu_3Ni_1 MAs and Cu_3Ni_1 NPs.

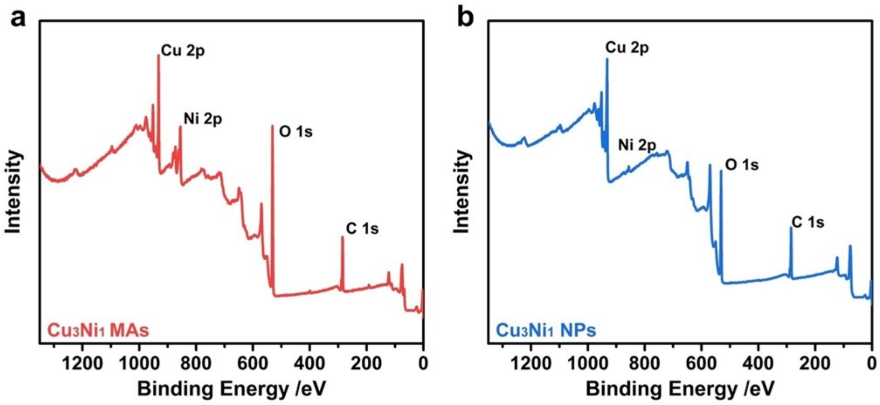

Fig. S25. XPS survey of (a) Cu_3Ni_1 MAs and (b) Cu_3Ni_1 NPs.

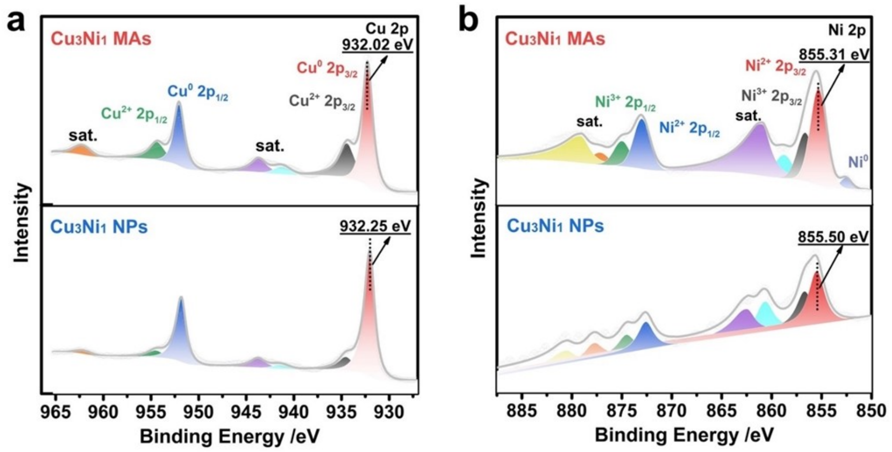

Fig. S26. High-resolution XPS spectra of (a) Cu 2p and (b) Ni 2p of Cu_3Ni_1 MAs and Cu_3Ni_1 NPs.

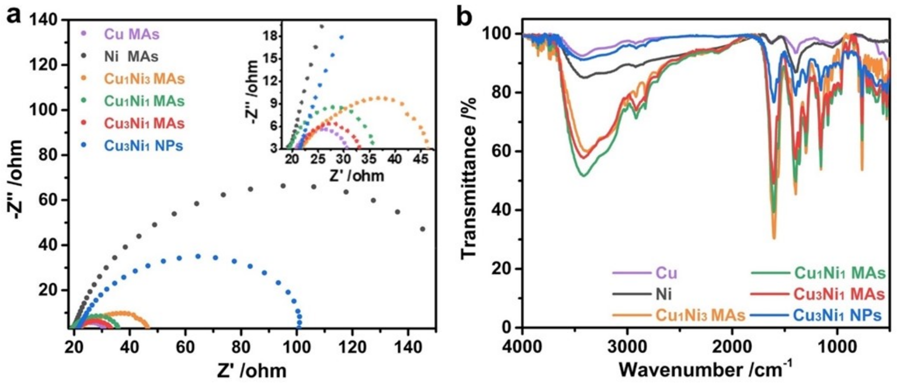

Fig. S27. (a) Nyquist plots, and (b) FTIR spectra of Cu MAs, Ni MAs, Cu_1Ni_3 MAs, Cu_1Ni_1 MAs, Cu_3Ni_1 MAs and Cu_3Ni_1 NPs.

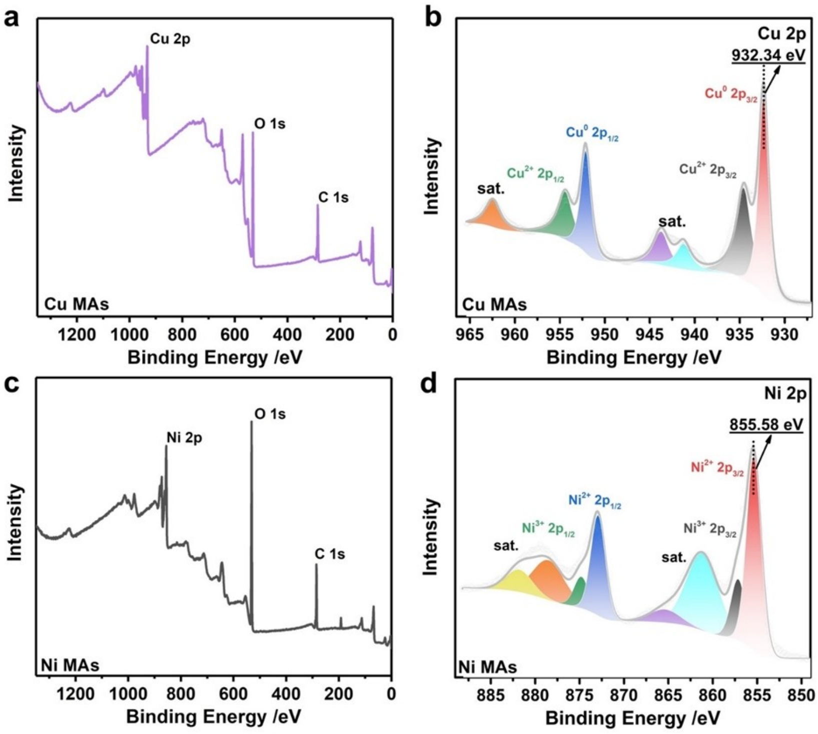

Fig. S28. (a, c) XPS survey and (b) Cu 2p spectrum, (d) Ni 2p spectrum of (a, b) Cu MAs and (c, d) Ni MAs.

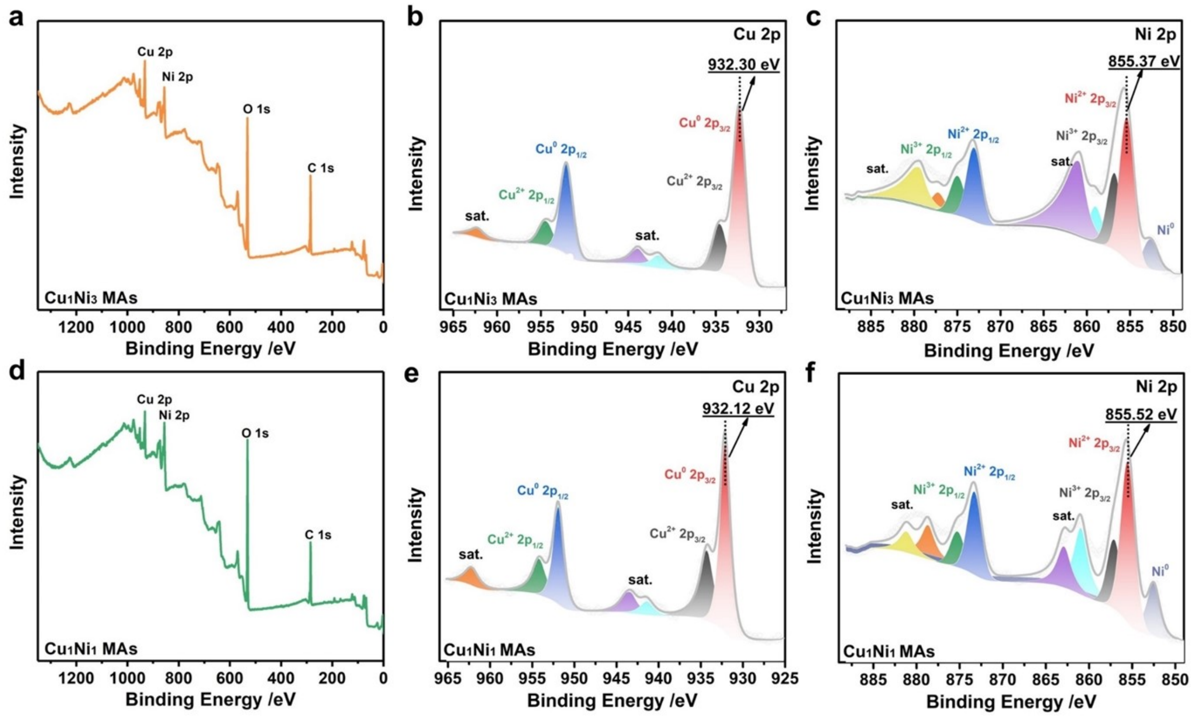

Fig. S29. (a, d) XPS survey, (b, e) Cu 2p spectrum and (c, f) Ni 2p spectrum of (a, b, c) Cu_1Ni_3 MAs and (d, e, f) Cu_1Ni_1 MAs.

Table S1. FE and selectivity of ethylamine obtained by electrochemical ARR of various reported electrocatalysts.

Catalysts	Electrolyte	FE (%)	Selectivity (%)	Ref.
Cu MAs	1 M NaOH	86.3	87.5	This work
Ni MAs		83.1	99.5	
Cu_1Ni_3 MAs		87.1	97.8	
Cu_1Ni_1 MAs		88	93.9	
Cu_3Ni_1 MAs		95.5	98	
Cu_3Ni_1 NPs		81.9	79.8	
Cu NPs	1 M NaOH	94.6	-	Nat. Commun. 2021, 12, 1949.
Ni NPs		80	-	
Pd NPs		66	-	
Cu Nanoarrays (NAs)/Cu Foil	0.5 M $KHCO_3$-CO_2	94	99	Chem Catal. 2021, 1, 393
	0.5 M $KHCO_3$-Ar	41	48	
Ni NAs/Cu Foil	0.5 M $KHCO_3$-CO_2	72	75	
[Co (DDP) $(H_2O)_2$] $(NO_3)_2$	0.1M $[N(C_4H_{9\text{-}n})_4]BF_4$-$N_2$	22	-	Dalton Trans. 2019, 48, 9576
[Co (cis-DDOP) (NO_3)] (NO_3)		11	-	
Pt black	1 M CH_3CN + 1 M NaOH	40	-	ACS Appl. Mater. Interfaces 2021, 13, 55292
Co_3B_1 amorphous alloy	10 mL CH_3CN + 30 mL EtOH	-	53	J. Catal. 2003, 214, 15
Co_3B_1 amorphous alloy-773 K		-	44.6	
Raney Co		-	38.8	
Ni_4B_1 amorphous alloy		-	24	
Ni_3B_1 amorphous alloy		-	28	
Ni_2B_1 amorphous alloy		-	37	
Raney Ni		-	21.4	

References

1. G. Kresse and J. Furthmüller, *Com. Mater. Sci.* 1996, **6**, 15-50.
2. G. Kresse and J. Furthmüller, *Phys. Rev. B* 1996, **54**, 11169-11186.
3. J. P. Perdew, K. Burke and M. Ernzerhof, *Phys. Rev. Lett.* 1996, **77**, 3865-3868.
4. G. Kresse and D. Joubert, *Phys. Rev. B* 1999, **59**, 1758-1775.
5. S. Grimme, J. Antony, S. Ehrlich and H. Krieg, *J. Chem. Phys.* 2010, **132**, 154104.
6. H. J. Monkhorst and J. D. Pack, *Phys. Rev. B* 1976, **13**, 5188-5192.